

First predictive simulations for deuterium shattered pellet injection in ASDEX Upgrade

M Hoelzl¹, D Hu², E Nardon³, GTA Huijsmans^{3,4}, the JOREK Team⁶, and the ASDEX Upgrade Team^{1,5}

¹Max Planck Institute for Plasma Physics, Boltzmannstr. 2, 85748 Garching b. M., Germany

²School of Physics, Beihang University, Beijing, 100191, China

³CEA, IRFM, 13108 Saint-Paul-Lez-Durance, France

⁴Eindhoven University of Technology, P.O. Box 513, 5600 MB Eindhoven, The Netherlands

⁵See the author list of H. Meyer et al. 2019 Nucl. Fusion 59 112014

⁶See <https://www.jorek.eu> for a current list of team members

Abstract

First predictive simulations of deuterium shattered pellet injection (SPI) into an ASDEX Upgrade H-Mode plasma obtained using the non-linear extended MHD code JOREK are presented. It is evaluated how various physical parameters corresponding to the plasma and to the SPI injection affect the MHD activity and thermal quench (TQ) dynamics. The influence of MHD activity onto the ablation of the pellet shards is shown to be crucial. A TQ is obtained quickly after injection in many simulations with a typical TQ duration of 100 microseconds. In the considered case with an initial central safety factor above unity, the core TQ takes place in the absence of a $q=1$ rational surface. Although the $n=1$ magnetic perturbation energy dominates in all simulations (single injection), toroidal harmonics up to $n=10$ provide an important contribution to the stochastization and to the stochastic transport in the plasma core. Right after the TQ, the density profile remains hollow for a few hundred microseconds. However, at the time when intact flux surfaces re-form around the magnetic axis, the density has become monotonic again suggesting a beneficial behaviour for runaway electron avoidance/mitigation. With 10^{21} atoms injected, the TQ is typically incomplete and triggered when the pellet shards reach the $q=2$ rational surface. At a larger number of injected atoms, the TQ can set in even before the shards reach this surface. For the low field side injection considered here, a repeated formation of strong outward convection cells is observed in the ablation region. This results from a sudden rise of the pressure in the high density cloud whenever the stochastic region expands further inwards such that heat is released from the hot plasma core. After the thermal quench, strong sheared poloidal rotation is created by Maxwell stress, which contributes to the re-formation of flux surfaces by decoupling modes at different rational surfaces. An outlook to future work is given.

Contents

1	Introduction	2
2	Simulation Setup	3
3	Results	6
3.1	Convergence	8
3.2	Ablation with a changing background	8
3.3	Particle content	10
3.4	Thermal quench	10
3.5	Evolution of poloidally and toroidally averaged profiles	13
3.6	Evolution of density, temperature, plasma flows, and magnetic topology across the thermal quench	15
4	Conclusions and Outlook	17
5	Acknowledgements	18

1 Introduction

Shattered pellet injection (SPI) is the basis of the planned ITER disruption mitigation system [1]. Although various experimental studies have been carried out for SPI in the last decade in particular at DIII-D [2–4] and although further tokamak devices are being equipped with SPI systems presently – an SPI system is also planned for the ASDEX Upgrade tokamak studied in this article –, still a lot of uncertainty remains about how such a system needs to be designed for ITER in order to mitigate all negative consequences of a disruption efficiently at the same time. In particular, eddy and halo current forces need to be kept within the limits of the supporting structures, more than 90% of the thermal energy needs to be radiated – also a large fraction of the magnetic energy converted to thermal energy during the current quench –, and the formation of a runaway electron beam needs to be avoided (or mitigated if avoidance is not possible). To match these requirements, among other constraints, the current quench (CQ) time will have to stay between particular upper and lower limits and the plasma density needs to increase by more than an order of magnitude across the whole plasma domain before intact flux surfaces begin to form again such that runaway electrons are confined in the plasma.

Besides NIMROD [5] and M3D-C1 [6], the JOREK code used for the present study is among the limited number of extended non-linear MHD codes world-wide, which has the necessary ingredients for simulating all aspects of mitigated disruptions in realistic geometry. Previous studies for massive gas and shattered pellet injection [7–12] demonstrate some of the capabilities. The code allows also to study the dynamics of runaway electrons [13, 14] and vertical displacement events [15, 16] which are closely related to (mitigated) disruptions. In the present article, only a small subset of the code features

is invoked to perform first predictive simulations for deuterium SPI into an ASDEX Upgrade H-mode plasma. While impurity SPI will play a crucial role for ITER, also deuterium SPI might be directly relevant for disruption mitigation. Such injections could allow to increase the plasma density and decrease the plasma temperature already before a thermal quench is triggered. This might be a way for mitigating both the runaway electron hot tail primary source and avalanche secondary source.

Clearly, a few aspects of the simulations will need to be further refined in the future, in particular when a lab characterization of the shard cloud becomes available for the ASDEX Upgrade injector. However the present simulations already give considerable insights into the expected dynamics and the features of the MHD activity. In the present study, various simulations are performed and analyzed to shed light onto the dependencies of the dynamics onto plasma and injection parameters. In Section 2, we describe the simulation setup used for our studies including a discussion of present limitations. Section 3 analyzes the various simulations and highlights key observations. Finally, Section 4 gives a physical interpretation of the results, and provides an outlook to more advanced simulations planned in the future.

2 Simulation Setup

The simulations shown in this article are performed with the JOREK¹ non-linear extended MHD code [17–19] using the energy conserving reduced MHD model [20] with the extension for neutral particles [8] and the model for shattered pellet injection and ablation [11]. The following scalar variables are evolved in time: Poloidal magnetic flux Ψ , electric potential u , toroidal current density j , toroidal vorticity ω , plasma density ρ , temperature T , parallel velocity v_{\parallel} , and neutrals density ρ_n .

A typical ASDEX Upgrade H-mode plasma is studied with a toroidal magnetic field amplitude of 2.5T, a toroidal plasma current of 0.8MA, a safety factor q of about 1.2 at the magnetic axis and about 5.8 at $\Psi_N = 0.95$, where $\Psi_N = (\Psi - \Psi_{\text{axis}})/(\Psi_{\text{separatrix}} - \Psi_{\text{axis}})$ denotes the normalized poloidal flux. The initial core temperature is about 3 keV, electron and ion temperatures are assumed to be equal for simplicity, and the core electron density in the deuterium plasma is about $8 \cdot 10^{19} \text{ m}^{-3}$. Deuterium SPI is simulated from the low field side (LFS) mid-plane into the plasma at a vertical location of $Z = 0.05$, which is equivalent to the vertical position of the magnetic axis.

Simulations are carried out with a Spitzer-like temperature dependent resistivity $\eta = \eta_0 (T/T_0)^{-3/2}$, where T_0 denotes the initial plasma core temperature. Since the goal of this study is to perform a comparably large number of simulations and investigate the dependency of the plasma behaviour onto various SPI parameters, most simulations are performed at a resistivity of $\eta_0 = 2 \cdot 10^{-7} \Omega\text{m}$ to limit computational costs. A single simulation is performed with a resistivity lower by a factor of ten, which approximately matches the experimental value (when taking into account neoclassical corrections; the resistivity is presently a function of the temperature only such that the radial dependency

¹Code version 2.19.05.0 is used along with the modifications for the shattered pellet injection and ablation model [11].

of the neoclassical corrections is not accounted for).

We concentrate on the following main questions: What impact does the MHD activity have onto pellet ablation and density increase in the plasma core? Which parameters determine whether a TQ is triggered by the SPI and when does the TQ occur? Can we identify an approximate threshold in the amount of injected material for obtaining a TQ? Which characteristic features are observed during the TQ? How does the density profile evolve during and after the TQ? How much does the core plasma density increase before re-formation of flux surfaces?

Since most of these questions are related to the early evolution of the plasma before and during the early TQ, which should be dominated by dilution and stochastic losses in case of pure deuterium injection [10], background impurity radiation is not considered. For this reason, the post-TQ temperatures will not be fully realistic in all simulations, but the values still allow to distinguish between full and incomplete TQ. For the same reason of focusing on the pre-TQ and TQ phases, vertical stability is not of interest here, such that all simulations are performed in a fixed boundary setup.

The shard cloud is simplified and additional effort in matching experimental properties will be carried out in the future, when a lab characterization of the shard cloud becomes available for the planned ASDEX Upgrade injector. All shards are assumed to have the same size for simplicity (see below for the number of atoms injected and the number of pellet shards simulated). The pellet shards are assumed to move straight with a constant velocity. The individual pellet shards are modelled as neutrals sources with Gaussian shape (in R , Z , and ϕ directions) moving with a velocity v_{SPI} into $-\mathbf{e}_R$ direction, which is 250 m/s in most simulations, plus a random velocity spread of 80 m/s (in simulations with a single pellet, no spread is applied, of course). The ablation model from Ref. [21] is used. The injection trajectory passes through the magnetic axis. The size of the Gaussian source in the poloidal plane is 8 cm and the localization in toroidal direction is 30 degrees . While the increased size of the shards in the simulations has an influence onto the simulations, also experimentally the ablation cloud is larger than the shards themselves. Furthermore, deuterium SPI is known to contain a large fraction of gas and particularly small shards, which increases the effective size of the ablation cloud. Finally, also turbulent transport, which may be driven by the locally enhanced gradients and might only partially be captured by the MHD model will reduce the localization of the pellet cloud perturbation. Nevertheless, a more accurate modelling of the shard cloud is envisaged for future ASDEX Upgrade studies, once its experimental properties are known.

The parallel heat diffusion coefficient $\chi_{||}$, is modelled with Spitzer-Härm [22] temperature dependency as $\chi_{||,0} (T/T_0)^{5/2}$. Here, the coefficient $\chi_{||,0}$ is typically taken to be $1 \cdot 10^{11}\text{ m}^2/\text{s}$, but $\chi_{||}$ is always restricted to a maximum value of $0.1\chi_{||,0}$. Consequently, $\chi_{||}$ becomes temperature independent at temperatures above this threshold, while the temperature dependency in colder regions is fully retained in the simulations. This choice is taken both for numerical reasons and to avoid an over-estimation of the core parallel conductivity, i.e., it is a strongly simplified way of accounting for the so-called heat flux limit [23]. Background flows of the initial plasma are not considered at present,

since a strong braking of the plasma rotation is expected anyways due to a “locking” of the island O-points to the injection location, which has been reported both theoretically and experimentally². For future simulations aiming at one to one comparisons with experiments, also the effect of the background rotation will be evaluated.

To gain insights into the triggering of the TQ by the injected material, the following parameters are varied in our simulations to investigate trends:

- While most simulations are carried out at $\eta_0 = 2 \cdot 10^{-7} \Omega \text{ m}$ for computational reasons, a single simulation is performed at $\eta_0 = 2 \cdot 10^{-8} \Omega \text{ m}$, which approximately corresponds to the experimental value.
- The number of injected atoms n_{atoms} is varied between the values 10^{21} , $3 \cdot 10^{21}$, and 10^{22} . If we assume, very roughly, that half of the material would be lost in the experiments before reaching the plasma, these parameters correspond to an initial pellet radius of about $2 \dots 4.5 \text{ mm}$ (assuming a spherical shape for simplicity and a density of $5 \cdot 10^{28} \text{ m}^{-3}$). The smallest number of atoms studied in this article is about five times larger than the largest ELM pacing pellets available in ASDEX Upgrade³. The plasma particle content before the injection is about $9.6 \cdot 10^{20}$ atoms.
- The number of pellet shards n_{shards} is varied in the simulations between the values 1, 3, 10, 30, 100. Thus, also the limit of an intact single pellet is captured.
- The material is injected into the plasma with a velocity $v_{\text{SPI}} = 250 \text{ m/s}$ in most cases. Two simulations are carried out at 150 m/s and 400 m/s for comparison. In all cases, the shards have a velocity spread of 80 m/s around the average velocity (except for the cases with only a single pellet, where only the nominal injection velocity is taken).
- The toroidal field amplitude $B_\phi = F_0/R$ is varied by the choice of the parameter F_0 , which has a value of 4.23 Tm in most cases, corresponding to 2.48 T on the magnetic axis. Two simulations are carried out at 2.34 T and 2.58 T , respectively, as a simple way of shifting the location of the $q = 2$ rational surface. Also in these simulations, the initial safety factor on axis remains above unity (to avoid the influence of an intrinsically unstable internal kink mode onto the simulations).
- The coefficient $\chi_{||,0}$ for the parallel heat transport is usually set to $1 \cdot 10^{11} \text{ m}^2/\text{s}$ in the simulations (see above for details on the model), however two simulations are carried out at 50% and 25% of that value, for comparison.

²Separate tests in a rotating ASDEX Upgrade X-point plasma with massive gas injection, which are not shown in this article, have confirmed, that the rotation can have a stabilizing impact if the amount of material is marginal for triggering a TQ in the absence of rotation. Under such conditions, the magnetic islands may not fully lock to the perturbation by the material injection and their rotation velocity may undergo cycles of deceleration while growing and acceleration while shrinking. When the amount of injected material is higher, the influence of the initial background rotation drops.

³ELM pacing pellets in ASDEX Upgrade have $1.5 \dots 3.7 \cdot 10^{20}$ atoms [24]. Also here, the amount of material actually reaching the plasma after the 17 m long guide tube is reduced considerably compared to this initial particle content.

- The number of Bezier finite elements n_{elems} is about 9k in most simulations, but has been increased to about 15k in some cases to confirm convergence.
- The toroidal Fourier harmonics included in the simulations typically cover $n = 0 \dots 10$, but some simulations have been performed with $n = 0 \dots 5$ and $0 \dots 15$ to confirm convergence.
- Furthermore, a few simulations were carried out with an artificial current source. In these cases, the resistivity acts only on $j - j_0$ instead of acting onto the total current j , where j_0 denotes the initial current profile. Including this current source term allows to keep the background current profile nearly constant. Comparing cases with and without this current source term therefore reveals the influence of the background current profile change onto MHD mode destabilization.
- An additional scan was performed modifying the injection geometry: case O (see Table 1) was repeated with an injection 5, 10, 15, and 20 cm above the magnetic axis location to study the sensitivity of the MHD response with respect to off-axis injection. The results in terms of ablation, magnetic energy perturbations, and core temperature evolution are very similar to the base case with the injection directly towards the magnetic axis. For this reason, the results of this scan are only mentioned here and the data is not included in the publication.
- To evaluate the impact of MHD activity onto the pellet shard ablation, additional simplified simulations were carried out. In the first one, the electric and magnetic fields are fixed in time such that MHD modes cannot develop and stochastic losses of thermal energy are excluded (Ψ , u , j are kept fixed). Consequently, dilution is the only relevant mechanism changing the temperature. In the second case, also the temperature (variable T) is kept fixed in time to investigate how ablation is affected by the change of the temperature due to dilution, parallel conduction, and MHD activity. In the third simulation, the complete background plasma is kept fixed in time during the ablation to mimic simplistic models sometimes used for pellet ablation estimates.

Table 1 lists the key parameters of all simulations that are analyzed in Section 3. A few further simulations were performed in the preparation of this study, but are not shown here. In particular simulations with $1 \cdot 10^{22}$ atoms injected are sometimes hard to continue across the TQ due to numerical convergence issues, possibly even higher grid resolutions might be required for such simulations in the future.

3 Results

In this Section, the simulation results are analyzed. Subsection 3.1 discusses the numerical convergence of the simulations. Subsection 3.2 investigates the impact of MHD activity onto the pellet ablation. Subsection 3.3 analyzes the evolution of the plasma particle content across the simulations. Subsection 3.4 studies key properties of the

	n_{at}	n_{sh}	η_0	v_{in}	$\chi_{ ,0}$	B_ϕ	n_{el}	N_{t}	j_0	fixed
A	.1	30	2	.25	1	2.48	9	10	yes	
B	.1	30	2	.15	1	2.48	9	10		
C	.1	30	2	.25	1	2.48	9	10		
D	.1	30	2	.4	1	2.48	9	10		
E	.3	1	.2	.25	1	2.48	15	10		
F	.3	1	2	.25	1	2.48	9	10		
G	.3	1	2	.25	1	2.48	15	5		
H	.3	1	2	.25	1	2.48	15	10		
I	.3	1	2	.25	1	2.48	15	15		
N	.3	3	2	.25	1	2.48	9	10		
Np	.3	3	2	.25	1	2.48	9	10	(yes)	Ψ, j, u, ω
NpT	.3	3	2	.25	1	2.48	9	10	(yes)	Ψ, j, u, ω, T
NpTr	.3	3	2	.25	1	2.48	9	10	(yes)	all
O	.3	30	2	.25	1	2.48	9	10		
P	.3	100	2	.25	1	2.48	9	10		
S	1	10	2	.25	1	2.48	9	10		
T	1	30	2	.25	.25	2.48	9	10		
U	1	30	2	.25	.5	2.48	9	10		
V	1	30	2	.25	1	2.48	9	10		
W	1	100	2	.25	1	2.48	9	10		
X	1	100	2	.25	1	2.34	9	10		
Y	1	100	2	.25	1	2.58	9	10		

Table 1: An overview is given of the parameters used for all simulation cases investigated in this study. The following information is shown: n_{at} is the number of atoms in the pellet in units of 10^{22} , n_{sh} represents the number of pellet shards, η_0 is the initial core resistivity in units of $10^{-7} \Omega\text{m}$, v_{in} is the injection velocity in units of km/s, $\chi_{||,0}$ the parallel conductivity coefficient in units of $10^{11} m^2/s$, B_ϕ denotes the toroidal field strength on axis in units of T, n_{el} gives the number of grid elements in units of 1000, N_{t} refers to the largest toroidal mode number included in the simulation, j_0 indicates whether a source is applied to keep the current profile approximately constant in time. In the column “fixed”, those variables are listed, which are kept constant in time. Parameter values deviating from the values used in most simulations are highlighted in bold print.

thermal quench observed in the simulations. Subsection 3.5 analyzes the evolution of poloidally and toroidally averaged profiles. And finally, Subsection 3.6 describes and compares the detailed dynamics across selected representative simulations.

3.1 Convergence

Before analyzing the results of the simulations, a few basic tests are performed to confirm numerical convergence. The poloidal and toroidal resolutions and the size of the time step were varied and to confirm that the results are converged very well in the perturbed magnetic energies during the non-linear evolution. Hyper-resistivity and hyper-viscosity are included for numerical reasons only with very small coefficients and scans in both parameters confirmed that the physical results are not affected by these parameters. For cases with $\eta = 2 \cdot 10^{-7} \Omega\text{m}$, a resolution of $n = 0 \dots 10$ and 9k grid elements is sufficient. As an example, the $n = 0 \dots 5$ magnetic energies of a case with 9k grid elements and the harmonics $n = 0 \dots 5$ included in the simulation are compared to a case with 15k grid elements and $n = 0 \dots 15$ included in the simulation. As visible from Figure 1, very good agreement is observed before, during, and after the TQ. In production simulations, nevertheless, a toroidal resolution of $n = 0 \dots 10$ is used in the following, since toroidal mode numbers up to 10 may still contribute considerably to the stochastic radial transport although they are strongly sub-dominant. For cases with a resistivity of $2 \cdot 10^{-8} \Omega\text{m}$, 15k grid elements are required for numerical stability reasons, while the toroidal resolution requirement does not change.

Furthermore, a few tests were carried out to verify the dependence of the results onto the plasma resistivity. Due to the computational costs, only few of those cases were run into the TQ at fully realistic resistivities. The tests show that results early in the simulation when ablation starts, are close together. However at the lower resistivity, the subsequent rise of the magnetic perturbation takes place slower and the TQ is delayed. Also, the amount of material needed to trigger a TQ is higher at lower resistivity. The tests confirm, that the plasma dynamics at increased resistivity values are similar to the dynamics at realistic values, however a lower number of atoms is sufficient for causing an MHD response of comparable amplitude. The available data indicates that about two to three times more material is needed for triggering the TQ at fully realistic resistivity compared to the ten times higher resistivity used in most simulations. This corresponds to an increase of the (spherical) pellet radius by 20...40%. Further simulations at fully realistic parameters will be carried out in the future, when the specification of the ASDEX Upgrade injector are fully known and presently ongoing optimizations of the solver have increased the computational efficiency for simulations with high resolution.

3.2 Ablation with a changing background

To investigate how the change of the temperature (and density) during injection affects the ablation of the pellet shards, several simulations were performed with the same equilibrium and pellet parameters. Besides a fully consistent MHD simulation (case N; see parameters in Table 1), three additional simulations are performed, where the model

		Temperature						Density			
		dil.	χ_{\perp}	χ_{\parallel}	v_{\perp}	v_{\parallel}	P_{Ohm}	D	v_{\perp}	v_{\parallel}	S_{SPI}
N	(MHD)	y	y	y	y	y	y	y	y	y	y
Np	(B fixed)	y	y	(y)	-	(y)	y	y	-	(y)	y
NpT	(B, T fixed)	-	-	-	-	-	-	y	-	(y)	y
NpTr	(all fixed)	-	-	-	-	-	-	-	-	-	-

Table 2: The tables shows which of the relevant terms, that can affect the temperature and density distributions, are retained in the four simulations considered in Section 3.2. Here “y” indicates that the term is retained, “(y)” indicates that the term is retained without reflecting stochastic transport since the magnetic field is kept fixed in time, and “-” indicates that the term is not present in the simulation.

was successively simplified. In case Np, the setup is identical to case N, however the electric field is zero and the magnetic field remains constant throughout the simulation. In case NpT, also the temperature is kept fixed in time. And finally in case NpTr all variables are kept constant in time such that the ablation is calculated in the absence of any perturbations of the initial plasma state.

The temperature in the MHD simulation can change due to the ionization energy (negligible for deuterium), radiation (negligible for deuterium), dilution, perpendicular diffusion, parallel diffusion, perpendicular convection, parallel convection and Ohmic heating. The density can change due to parallel and perpendicular convection, isotropic diffusion, ionization of neutrals (the pellet shard source), and recombination (negligible). Table 2 shows which of the terms are retained in the four cases considered here. From case N to case Np perpendicular convection and stochastic transport are dropped, which does not allow a true thermal quench to occur any more. From case Np to NpT all changes of the temperature are dropped while the density can still evolve. And finally case NpTr reflects ablation in the presence of a completely static background. Figure 2 compares the ablation rates and shard sizes in the four cases during the injection. The location of the shard cloud is shown on the X-axis, injection is from the right.

In the very beginning of the injection, the shards are located in a cold plasma region (SOL or pedestal bottom) such that ablation is slow. However, in case N, where stochasticization of the plasma edge sets in quickly, heat from the pedestal is released along the magnetic field lines into the SOL region such that ablation increases in this case compared to the other simulations. Case NpT with successively shows the fastest ablation, since the density can increase by the ablation (which enhances ablation in turn), but the temperature remains unperturbed. The injection with completely fixed background (case NpTr) exhibits only slightly lower ablation rates than case NpT, which is related to the rather weak dependency of the ablation rate on the density. Case Np initially shows very similar ablation to the fully consistent MHD simulation (case N). However, this changes when the TQ sets in: Ablation in case N drops quickly following the core TQ onset, since the temperature has dropped, while ablation in case Np remains high

until complete ablation since an MHD driven thermal quench is not present in that case (temperature only drops by dilution). Due to the absence of impurity background radiation, post-TQ temperatures are overestimated in the simulations, such that case N still exhibits a small ablation rate after the TQ. Either way, the shards in case N are not fully ablated and the remaining material would eventually hit the plasma facing components on the opposite side of the injection location.

3.3 Particle content

In this Section, the evolution of the particle content is compared across various simulations. Figure 3 shows the time evolution of the particle content for many different simulations versus time. Clearly, the amount of injected material and the number of shards influence strongly, how much material is assimilated. Case W with $1 \cdot 10^{22}$ atoms injected in 100 shards exhibits the strongest increase of the particle content, by a factor of almost 4.5. Most simulations are stopped right after the TQ to save computational time (they could be continued). For those cases which have been continued further, finite ablation is still observed after the TQ. However, with background impurity radiation included, the post-TQ temperature would be lower in most cases (likely not case C, which is characterized by an incomplete TQ) such that ablation would come to an end.

In Figure 5, five comparisons are shown. Each plot shows a set of simulations which are identical except for a single parameter. It can be seen that the influence of the toroidal resolution, the resistivity, and the toroidal field strength is negligible. However, the injection velocity strongly influences the particle content, since the shards can reach plasma regions with higher temperatures faster where ablation is enhanced. The maximum particle content is strongly increased for higher injection velocities. Also the parallel heat diffusion coefficient plays an important role since a larger “reservoir” of thermal energy is available for ablation if the transport is faster. While the difference between the simulation with fully realistic conductivity, and the simulation with half of this value is small, the simulation with further reduced parallel heat conductivity shows a strongly delayed ablation. The origin for this behaviour is that at lower parallel conductivities, the temperature is not equilibrated as quickly any more within a flux surface, which reduces the temperature near the ablation cloud and therefore reduces ablation. This reduced ablation is “self-reinforced” by the following effect. An initially smaller ablation rate means that the overall temperature drop in the flux surface by dilution is lower, leading to a weaker steepening of the current profile, which in turn reduces the drive for MHD modes and slows down the formation of a stochastic region. In addition, lower parallel conductivities also decrease the stochastic radial losses directly.

3.4 Thermal quench

This Section compares the TQ onset times and durations across the whole set of simulations. A first rise of magnetic energies to significant amplitudes is observed already at a simulation time of about 0.15 ms corresponding to the excitation of edge instabilities, which lead to a stochastization of the edge plasma and a loss of the edge plasma

case	$t_{\text{TQ start}}$	Δt_{TQ}	$T_{\text{post TQ}}$
A	(no TQ before 1.30ms)		
B	(no TQ before 1.45ms)		
C	931	316	27%
D	527	119	18%
E	1176	591	5%
F	859	91	12%
G	851	95	11%
H	860	45	13%
I	883	40	14%
N	709	96	10%
O	596	95	9%
P	576	100	8%
S	594	?	?
T	703	236	5%
U	576	108	9%
V	565	114	5%
W	516	75	6%
X	455	323	6%
Y	515	124	5%

Table 3: An overview is given of the TQ behaviour for the cases of Table 1. For those cases which show a core TQ, the TQ onset time and the TQ duration are given in μs . The TQ onset is defined as the point in time, at which 5% of the fast core temperature drop has completed, and the TQ completion is the time when 95% of the core temperature drop has taken place. The post TQ temperature is given as a fraction of the initial core temperature, which is around 3 keV in the considered equilibrium.

confinement. This happens almost immediately, when the first shards reach the plasma boundary. Thus, an “edge TQ” is observed very quickly after injection, very likely the high sensitivity of the plasma to this perturbation is caused by the steep pedestal profiles of the H-mode plasma considered here. The edge crash has similarities to pellet triggered ELMs, however the triggering is greatly accelerated by the large amount of injected material in this study. The evolution of magnetic perturbation energies and Poincaré plots are shown in Section 3.6.

The “core TQ” sets in around $0.5 \dots 1$ ms in the simulations, and completes within typically 0.1 ms like shown in Table 3 and seen from Figure 4. The magnetic perturbation energies during the TQ are higher by about one order of magnitude compared to those of the edge crash. Such time scales are far faster than the resistive time scale and are an indication for fast magnetic reconnection taking place during the core TQ [25]. This aspect will be analyzed and discussed in a separate study in depth. Close to the threshold for obtaining a TQ (e.g., by reducing the amount of injected atoms), the TQ duration increases strongly and the TQ may become incomplete with post-TQ temperatures $> 10\%$. Like mentioned before, the post-TQ temperature is not captured fully accurately in the present simulations, since, for instance, radiative cooling by background impurities is not taken into account. However, the post-TQ temperature is still a good indicator showing whether stochastization is strong enough and/or long-lived enough to create a full TQ, or only a partial TQ (in case of a partial TQ, the temperatures are still so high that background impurity radiation might not be particularly effective; however this of course depends also on the impurity species considered). In this study, only a core TQ shortly after injection is considered. Plasmas which are not quenching that quickly might still develop a TQ later on. On the other hand, a plasma undergoing an incomplete TQ (like cases C, D), might recover later on. Such a longer term evolution of the plasma is not investigated in the present study.

In the simulations with 250 m/s injection velocity, the pellet shards reach the rational surfaces approximately at 0.3 ms ($q=4$), 0.45 ms ($q=3$), 0.8 ms ($q=2$), and 1.3 ms ($q=1.5$). Those numbers are calculated assuming that the q -profile does not change too much compared to the initial equilibrium. Due to actual changes of the equilibria, these times differ slightly between cases. A detailed comparison shows that these TQ onset times correspond to the shard cloud reaching the $q=2$ surface in cases with a lower amount of atoms or fewer shards (cases C and F/G/H/I).

In all cases with either more atoms or more shards, the TQ takes place already earlier. In cases N and T, the shards have crossed the $q = 2.5$ surface already, in cases O, P and U-Y, the shards have only gotten somewhere into the region of the $q = 3$ or $q = 2.5$ surfaces. Cases A-B do not show a TQ within the simulated time, however the pellet shards have already long been ablated before the end of these simulations.

Only in the simulation with $\eta = 2 \cdot 10^{-8} \Omega\text{m}$ and a single pellet with $3 \cdot 10^{21}$ atoms, the TQ onset is observed after the pellet has crossed the $q = 2$ surface. More atoms or shards would likely lead to an earlier TQ again.

In most cases, the core TQ completes within about 0.1 ms after the onset. A small amount of atoms (case C), or a low resistivity with few shards and a moderate number of atoms (case E) increase this time. In cases T and X, the TQ takes place in two

“steps” such that the overall duration seems longer, while the first crash is still faster than 0.1 ms.

The post-TQ temperature shows a strong dependency on the number of injected atoms (and also some dependency on the number of shards). In particular cases C and D exhibit only an incomplete TQ. At lower resistivity, the TQ onset is later and the TQ duration is considerably longer such that the post-TQ temperature is also low in this case.

Cases B, C, and D allow to compare different injection velocities. The slowest injection of 150 m/s does not show a TQ within the simulated time frame, the injection at 250 m/s shows a rather late and slow TQ, and the injection at 400 m/s shows an earlier and faster TQ leading to a slightly lower post-TQ temperature.

The comparison between case A and C shows the importance of changes in the current profile. Indeed, while case A (which has a current source tending to maintain the current profile) does not show a TQ, case C (which does not have the source term) shows a partial TQ when the shards reach the $q = 2$ surface. Consequently, the steepening of the current profile caused by the edge cooling is an important factor in the destabilization of the MHD activity leading to the TQ.

The effect of shifting the 2/1 rational surface can be investigated by comparing cases W, X, and Y. The results are not conclusive here, however. Possibly a scan with fewer atoms, where a stronger correlation of the TQ onset to the shards reaching the $q = 2$ surface was seen, would lead to a more conclusive picture. However, since the central safety factor is changing as well in this scan (the toroidal field strength is varied, while all other aspects of the equilibrium are kept the same), the comparison must be anyway seen as preliminary and is kept here only for completeness.

To investigate the impact of the parallel conductivity onto the plasma dynamics, the three cases T ($\chi_{||,0} = 2.5 \cdot 10^{10} \text{ m}^2/\text{s}$), U ($5 \cdot 10^{10} \text{ m}^2/\text{s}$), and V ($1 \cdot 10^{11} \text{ m}^2/\text{s}$) are considered. Ablation takes place significantly slower in case T compared to the other two cases as seen in Figure 5. As a result, T shows a delayed TQ and a slower TQ. Cases U and V show very similar ablation, TQ onset times, and TQ duration indicating that above a particular threshold, the parallel conductivity does not affect the MHD activity strongly any more. Nevertheless, the magnetic perturbation energy is higher in case V than in case U by a factor of almost two. Both, the higher perturbation amplitude (stronger stochastization) and the higher parallel conductivity act together to reduce the power-TQ temperature in case V to lower values than those of case U.

Figure 4 shows the evolution of the plasma core temperature and densities in comparison for several cases. This will be analyzed in more depth in the following Sections. In Section 3.5, the evolution of the background profiles is analyzed for particular cases, and finally in Section 3.6, the detailed distributions are investigated.

3.5 Evolution of poloidally and toroidally averaged profiles

In this section, the evolution of poloidally and toroidally averaged profiles is compared across several cases to highlight common properties and differences. Figures 6 to 10 correspond to the cases D, G, N, and W, which show an increasingly violent TQ. In each of these figures, the uppermost plot shows the evolution of the magnetic perturbation

energies versus time. The second plot shows the evolution of the density profile versus time. The third plot shows the evolution of the temperature profile versus time. The fourth plot shows the evolution of the current profile versus time. And the fifth plot shows the evolution of the q -profile versus time. The poloidally/and toroidally averaged quantities are plotted against the normalized poloidal flux (note that the definition of the normalized poloidal flux evolves slightly with time, since the magnetic field is changing). The white dotted line indicates the location of the center of mass of the SPI shard cloud.

Case D (10^{21} injected atoms, 30 shards, 400 m/s). As shown in Figure 6, ablation completes when the shard cloud reaches the $q=2$ surface approximately. The core TQ takes place roughly at this time as well. An incomplete TQ is observed with a high post-TQ temperature and moderate density increase mostly outside the $q = 2$ surface. The magnetic $n=2$ energy increases strongly when the core TQ takes place, while the $n=1$ energy stays roughly constant. The coupling to the higher harmonics is not strong. The current profile peaks a bit after the TQ, but not strongly enough for a $q = 1$ surface to appear. This peaking of the current after the TQ appears since the edge is cooled first and the current is lost from the stochastic region and re-induced in the still hot plasma center like described in Ref. [26]. The q -profile is altogether only weakly perturbed. Following the core TQ, a high temperature “plume” is visible in the temperature profile, moving outwards across the whole plasma on a fast timescale by stochastic energy transport. This leads to a significant re-heating of the outer plasma region.

Case G ($3 \cdot 10^{21}$ injected atoms, single shard, 250 m/s). As shown in from Figure 7, the TQ approximately takes place, when the shard cloud reaches the $q=2$ rational surface. The post TQ temperature is lower than the one of case D, but still relatively high indicating a partial TQ. Density increases still after the TQ, but mostly outside the location of the shard cloud. The magnetic $n=2$ and $n=3$ amplitudes increase strongly when the core TQ occurs, also $n=1$ is growing but not as sharply. A stronger coupling of the harmonics is observed. The current profile peaks and a $q=1$ surface appears in the very center. The plume of the outward temperature flow from the core TQ is again clearly visible and re-heats the plasma edge.

As shown in Figure 8, which shows the same data for the same case, but over a longer time window, strong bursts of MHD activity are seen again at about 1.9 ms and about 3.1 ms in the later evolution of case G. The burst at 1.9 ms appears roughly when q on axis drops below 1.5. After this crash, the $q=1.5$ and $q=2$ surfaces have disappeared and two $q=2.5$ surfaces are present due to a low axis current density. The $q=2.5$ surfaces finally merge and disappear around 2.8 ms, before the next burst appears around 3.1ms. This crash seems to appear, when one of the two $q=3$ surfaces reaches the plasma center. The plasma core density rises to very high values in this case, since ablation continues after the TQ due to the comparably high post-TQ temperature, and the series of MHD crashes leads to a strong convection across flux surfaces.

Case N ($3 \cdot 10^{21}$ injected atoms, 3 shards, 250 m/s). As shown in from Figure 9, the TQ appears approximately, when the shard cloud has reached the $q=2$ surface. The post TQ temperature is far lower than in the previous cases. Still the density continues to increase a bit after the TQ. During the TQ, the magnetic perturbation increases strongly across all harmonics due to strong mode coupling. The current profile peaks enough for a $q=1$ surface to appear shortly after the TQ in the very center of the plasma. The outward flowing heat is clearly visible in the temperature profile and shows a sub-structure which corresponds well to the evolution of the magnetic perturbation energies.

Case W (10^{22} injected atoms, 100 shards, 250 m/s). As shown in Figure 10, the TQ appears approximately when the shard cloud has reached the $q=2.5$ surface. A crash of the outer plasma core up to and including the $q=1.5$ surface is already observed when the shard cloud has reached the $q=3$ surface. The post TQ temperature is far lower in this case, however the density still increases slightly after the TQ even inside the location of the shard cloud due to a mixing effect. Both at the time of the crash of the outer plasma core and at the time of the core TQ, the magnetic energy of all harmonics rises in a tightly coupled way. An outflow of the thermal energy from the hot plasma region is seen already at 0.25ms moving slowly in the radial direction due to the moderate stochastization at that point in time. Later on, at the two major crashes (≈ 0.46 ms and ≈ 0.55 ms), the radial propagation velocity of the outflow is significantly higher. These radial propagation velocities approximately are 1 km/s, 10 km/s, and 20 km/s reflecting the different stochastization levels at these points in time. The current peaks after the TQ such that a $q=1$ surface is observed for a short while. Since a comparably fast current quench sets in due to the low post-TQ temperature, the q -profile starts to rises quickly after the TQ. In the following Section, case W is analyzed in more detail.

3.6 Evolution of density, temperature, plasma flows, and magnetic topology across the thermal quench

In this Section, case W, which shows a pronounced TQ (see Figure 10) is analyzed in detail. In particular, the evolution of density distribution, temperature distribution, plasma flows, and magnetic topology are investigated.

The magnetic topology before, during, and after the TQ can be seen in Figure 11. Poincaré plots are shown for several time points during the simulation. The first plot represents the unperturbed equilibrium. The second plot corresponds to $t = 0.357$ ms, where the whole edge region of the plasma is already stochastic up to the $3/2$ magnetic surface. The next time point $t = 0.441$ ms has a significantly higher $n = 1$ magnetic perturbation energy, while the higher harmonic perturbations have hardly changed. The stochastic region has not yet moved further inwards. At time point $t = 0.508$ ms, the $n = 2$ magnetic perturbation has strongly increased corresponding to a stochastization of the $3/2$ surface. Time point $t = 0.567$ ms during the core thermal quench shows stochastization of the complete plasma, however weak stochastization at the grid center. During the following two time points $t = 0.593$ ms and $t = 0.710$ ms the complete plasma domain is stochastic. Time point $t = 0.895$ ms corresponds to the onset of re-formation

of flux surfaces from the center. The last time point shown at $t = 1.013$ ms is weakly stochastic in the whole plasma core such that runaway electrons would not be lost easily any more from this region, if they were present. Island remnants are visible at this time point at various rational surfaces in the stochastic region.

Figure 12 displays the connection length to the divertor of several field lines started close to the (initial) magnetic axis. Before the TQ, the field lines are never lost, during and after the TQ the connection length can drop to a few hundred meters corresponding to less than 100 toroidal turns. However, even in the phase of strong stochastization, time points exist, where some field lines remain confined inside the plasma. This motivates further analysis in the future regarding runaway electron dynamics in such fields, to understand generation and losses of runaway electrons in such a plasma evolution (such as the work for massive gas injection simulations for JET reported in Ref. [13, 27]).

For the same time points as the Poincaré plots, Figure 13 shows the evolution of the density and temperature in a poloidal cross section. Strong 3D structures are present before the TQ. During the TQ and for $200\ \mu\text{s}$ after it, the density profile remains hollow. And about $400\ \mu\text{s}$ after the TQ, the core density has increased by a factor of about six compared to the initial equilibrium state. Favorably for runaway electron mitigation/suppression, the re-formation of flux surfaces seems to appear at a point in time, when the density profile is not hollow any more.

Figure 14 shows contours of the stream function u of the poloidal velocity for the same time points as those of Figures 11 and 13. Strong outwards oriented convection cells form at the location of the high density cloud several times during the simulation (a gradient of u pointing downwards corresponds to a convection in $+\mathbf{e}_R$ direction), hindering the penetration of the ablated material into the plasma core. These cells always form, when a significant amount of thermal energy is released from the hot plasma core, either by the core TQ itself, or by a loss of a layer of closed flux surfaces (inward motion of the stochastic front). It is observed particularly strongly between 0.47 ms and 0.59 ms. The convection cells are visible for instance the time points 0.508 ms and 0.567 ms in Figure 14 and are related to the plasmoid drifts described in Ref [28], which render assimilation of the material for LFS injection inefficient. For HFS injection, the corresponding interchange instabilities would lead to a material convection towards the plasma center instead, greatly increasing the assimilation of material at this stage of the simulation.

As seen from time points 0.567 ms and 0.593 ms, strongly localized convection cells form in the plasma center during the TQ. However, these cannot increase the core plasma density immediately, since they are spatially separated from the high density cloud, which had been pushed away by the interchange instability driven convection cell described above. After the TQ, strong poloidal rotation resulting from Maxwell stress is observed as seen from time point 0.710 ms. In addition, convection cells oriented towards the plasma center are now forming as seen from time points 0.710 ms and 0.895 ms, which leads to an increase of the core plasma density turning the hollow density profile again into a monotonic one. In addition, parallel transport with the ion sound speed in the stochastic field contributes to an increase of the core density. Together, these parallel and perpendicular transport mechanisms fill the hole in the density profile within about

0.2 ms after the TQ. About 0.4 ms after the TQ, the density distribution has become smooth and monotonic across the plasma and plasma flows have dropped to low values.

4 Conclusions and Outlook

First predictive simulations for deuterium shattered pellet injection into an ASDEX Upgrade H-mode plasma are shown. Various simulations were performed to study the influence of plasma parameters and injection parameters onto the results. In spite of some limitations of the present simulations (e.g., deuterium injection, neglected impurity background radiation, simplified modelling of the shard cloud, increased resistivity in most cases), significant insight into the MHD activity and TQ dynamics during SPI injection is obtained. The number of atoms injected, the number of pellet shards, the injection velocity, the plasma resistivity, and the parallel heat conductivity influence the dynamics strongly. An increase of each of these parameters generally is seen to act destabilizing such that the TQ occurs earlier, has a shorter duration, and causes a lower post-TQ temperature.

The influence of MHD activity onto the ablation of pellet shards was analyzed by comparing the self-consistent simulation with simplified simulations without MHD activity and a fixed background profile. The MHD activity strongly influences ablation, in particular due to stochastic heat transport from the originally confined region.

A loss of the plasma edge confinement is observed almost instantaneously when the pellet shards reach the plasma boundary, since an H-mode plasma is considered. The loss of edge plasma current and the corresponding steepening of the current profile are shown to affect the destabilization of MHD activity significantly. A thermal quench (TQ) is observed within the first millisecond after injection in almost all simulations and takes typically about 0.1 milliseconds. Compared to simulations for JET [11], the stochastic front is moving inwards a lot faster. This may be related to a different ordering between the shard propagation time scale and the time scale the current profile takes to adapt (the injection velocity is slower in the considered case, while the resistivity is higher).

At 10^{21} atoms injected, only incomplete TQs are observed, at $3 \cdot 10^{21}$ the crashes are more complete, and at $1 \cdot 10^{22}$ atoms the crashes are complete (low post-TQ temperature) and more violent. The shards have not crossed the $q=2$ rational surface before the TQ onset in almost all cases. The stochastic outflow of thermal energy from the plasma core leads to the formation of a convection cell in the high density ablation cloud oriented outwards for the low field side injection considered here, hindering an efficient penetration of the material into the core. The density profile has a strong 3D structure before and during the TQ. It remains hollow until about 0.1-0.2 milliseconds after the TQ. Successive mixing by small convection cells and inward transport by a large convection cell leads to a flat density profile later on. With 10^{22} atoms injected, an increase of the initial plasma core density by a factor of about six is observed. At the onset of the TQ, the magnetic topology becomes fully stochastic and the connection length of field lines to the divertor targets drops to few hundred meters. First flux surfaces in the core as well as island remnant surfaces begin to re-form a few hundred microseconds after the onset

of the TQ. This re-formation of flux surfaces is enforced also by strong poloidal rotation driven by Maxwell stress, in particular after the TQ. The re-formation of flux surfaces is observed at a point in time, when the density profile is not hollow any more, which is a promising observation for runaway electron mitigation or suppression.

Taking into account material losses before the pellet shards have reached the plasma edge, a less violent plasma response at fully realistic resistivity (which was used only in one simulation for computational reasons), and the stabilizing effect of plasma flows prior to the injection, an initial pellet size of around $(8 \pm 4) \cdot 10^{21}$ deuterium atoms is expected to cause a TQ in the experiment early after injection. A delayed TQ several milliseconds after injection would likely occur already with significantly smaller injection quantities (density limit disruption).

Future work will take into account impurity background radiation, plasma background flows, MHD activity existing before the injection, fully realistic plasma parameters, and be adapted for a planned lab characterization of the ASDEX Upgrade shard cloud. For impurity SPI, an extended impurity model will be implemented in JOEREK. Using the free boundary JOEREK-STARWALL code [29], also vertical stability and control will be taken into account and runaway electron dynamics will be studied using the models described in Refs. [13, 14]. Numerical improvements which are presently ongoing, are expected to reduce the computational costs and enhance numerical stability at fully realistic parameters. When first ASDEX Upgrade SPI experiments become available, one to one comparisons are planned.

5 Acknowledgements

Parts of this work has been carried out within the framework of the EUROfusion Consortium and has received funding from the Euratom research and training programme 2014-2018 and 2019-2020 under grant agreement No 633053. Parts of this work was carried out using the Marconi-Fusion supercomputer. The views and opinions expressed herein do not necessarily reflect those of the European Commission. The authors would like to acknowledge many fruitful discussions and the efficient code development in the JOEREK team. Helpful discussions with Gergely Papp, Gabriella Pautasso, Karl Lackner and Sibylle Günter are acknowledged.

References

- [1] M. Lehnen, K. Aleynikova, P.B. Aleynikov, D.J. Campbell, P. Drewelow, N.W. Eiditis, Yu. Gasparyan, R.S. Granetz, Y. Gribov, N. Hartmann, E.M. Hollmann, V.A. Izzo, S. Jachmich, S.-H. Kim, M. Kočan, H.R. Koslowski, D. Kovalenko, U. Kruezi, A. Loarte, S. Maruyama, G.F. Matthews, P.B. Parks, G. Pautasso, R.A. Pitts, C. Reux, V. Riccardo, R. Rocella, J.A. Snipes, A.J. Thornton, and P.C. de Vries. Disruptions in iter and strategies for their control and mitigation. *Journal of Nuclear Materials*, 463:39 – 48, 2015. ISSN 0022-3115. doi:[10.1016/j.jnucmat.2014.10.075](https://doi.org/10.1016/j.jnucmat.2014.10.075). PLASMA-SURFACE INTERACTIONS 21.

- [2] N. Commaux, L.R. Baylor, T.C. Jernigan, E.M. Hollmann, P.B. Parks, D.A. Humphreys, J.C. Wesley, and J.H. Yu. Demonstration of rapid shutdown using large shattered deuterium pellet injection in DIII-d. *Nuclear Fusion*, 50(11):112001, sep 2010. doi:[10.1088/0029-5515/50/11/112001](https://doi.org/10.1088/0029-5515/50/11/112001).
- [3] N. Commaux, D. Shiraki, L.R. Baylor, E.M. Hollmann, N.W. Eidietis, C.J. Lasnier, R.A. Moyer, T.C. Jernigan, S.J. Meitner, S.K. Combs, and C.R. Foust. First demonstration of rapid shutdown using neon shattered pellet injection for thermal quench mitigation on DIII-d. *Nuclear Fusion*, 56(4):046007, mar 2016. doi:[10.1088/0029-5515/56/4/046007](https://doi.org/10.1088/0029-5515/56/4/046007).
- [4] D. Shiraki, N. Commaux, L. R. Baylor, N. W. Eidietis, E. M. Hollmann, C. J. Lasnier, and R. A. Moyer. Thermal quench mitigation and current quench control by injection of mixed species shattered pellets in DIII-D. *Physics of Plasmas*, 23(6):062516, 2016. doi:[10.1063/1.4954389](https://doi.org/10.1063/1.4954389).
- [5] Charlson C. Kim, Yueqiang Liu, Paul B. Parks, Lang L. Lao, Michael Lehnen, and Alberto Loarte. Shattered pellet injection simulations with nimrod. *Physics of Plasmas*, 26(4):042510, 2019. doi:[10.1063/1.5088814](https://doi.org/10.1063/1.5088814).
- [6] N.M. Ferraro, B.C. Lyons, C.C. Kim, Y.Q. Liu, and S.C. Jardin. 3d two-temperature magnetohydrodynamic modeling of fast thermal quenches due to injected impurities in tokamaks. *Nuclear Fusion*, 59(1):016001, nov 2018. doi:[10.1088/1741-4326/aae990](https://doi.org/10.1088/1741-4326/aae990).
- [7] C Reux, G Huysmans, J Bucalossi, and M Becoulet. Non-linear simulations of disruption mitigation using massive gasinjection on tore supra. In *38th European Physical Society Conference on Plasma Physics (EPS), Strasbourg, France*, page O3.117, 2011. URL <http://ocs.ciemat.es/EPS2011PAP/pdf/O3.117.pdf>.
- [8] A. Fil, E. Nardon, M. Hoelzl, G. T. A Huijsmans, F. Orain, M. Becoulet, P. Beyer, G. Dif-Pradalier, R. Guirlet, H. R. Koslowski, M. Lehnen, J. Morales, S. Pamela, C. Passeron, C. Reux, and F. Saint-Laurent. Three-dimensional non-linear magnetohydrodynamic modeling of massive gas injection triggered disruptions in jet. *Physics of Plasmas*, 22(6):062509, 2015. doi:[10.1063/1.4922846](https://doi.org/10.1063/1.4922846). URL <http://dx.doi.org/10.1063/1.4922846>.
- [9] Alexandre Fil. *Modélisation des disruptions déclenchées par injection massive de gaz dans les plasmas de tokamaks*. PhD thesis, Aix-Marseille University, 2015. URL <http://www.theses.fr/2015AIXM4040>.
- [10] E Nardon, A Fil, M Hoelzl, G Huijsmans, and JET contributors. Progress in understanding disruptions triggered by massive gas injection via 3d non-linear MHD modelling with JOEKE. *Plasma Physics and Controlled Fusion*, 59(1):014006, 2017. URL <http://stacks.iop.org/0741-3335/59/i=1/a=014006>.

- [11] D. Hu, E. Nardon, M. Lehnen, G.T.A. Huijsmans, and D.C. van Vugt and. 3d non-linear MHD simulation of the MHD response and density increase as a result of shattered pellet injection. *Nuclear Fusion*, 58(12):126025, oct 2018. doi:[10.1088/1741-4326/aae614](https://doi.org/10.1088/1741-4326/aae614).
- [12] D Hu, E Nardon, G T A Huijsmans, M Lehnen, D C van Vugt, and JET contributors. JOREK simulations of shattered pellet injection with high Z impurities. In *45th European Physical Society Conference on Plasma Physics (EPS), Prague, Czech Republic*, page P4.1043, 2018. URL <http://ocs.ciemat.es/EPS2018PAP/pdf/P4.1043.pdf>.
- [13] C. Sommariva, E. Nardon, P. Beyer, M. Hoelzl, G.T.A. Huijsmans, and D. van Vugt and. Test particles dynamics in the JOREK 3d non-linear MHD code and application to electron transport in a disruption simulation. *Nuclear Fusion*, 58(1):016043, dec 2017. doi:[10.1088/1741-4326/aa95cd](https://doi.org/10.1088/1741-4326/aa95cd).
- [14] V. Bandaru, M. Hoelzl, F. J. Artola, G. Papp, and G. T. A. Huijsmans. Simulating the nonlinear interaction of relativistic electrons and tokamak plasma instabilities: Implementation and validation of a fluid model. *Phys. Rev. E*, 99:063317, Jun 2019. doi:[10.1103/PhysRevE.99.063317](https://doi.org/10.1103/PhysRevE.99.063317).
- [15] Francisco Javier Artola Such. *Free-boundary simulations of MHD plasma instabilities in tokamaks*. PhD thesis, Université Aix Marseille, 2018. URL <https://hal-amu.archives-ouvertes.fr/tel-02012234v1>.
- [16] I Krebs, F J Artola, C R Sovinec, S C Jardin, K Bunkers, M Hoelzl, and N M Ferraro. Axisymmetric simulations of vertical displacement events: A benchmark of nonlinear MHD codes. *Physics of Plasmas*, XXX:submitted, 2019. preprint at <https://arxiv.org/abs/1908.02387>.
- [17] G.T.A. Huysmans and O. Czarny. MHD stability in x-point geometry: simulation of ELMs. *Nuclear Fusion*, 47(7):659, 2007. doi:[10.1088/0029-5515/47/7/016](https://doi.org/10.1088/0029-5515/47/7/016).
- [18] Olivier Czarny and Guido Huysmans. Bezier surfaces and finite elements for MHD simulations. *Journal of Computational Physics*, 227(16):7423 – 7445, 2008. ISSN 0021-9991. doi:[10.1016/j.jcp.2008.04.001](https://doi.org/10.1016/j.jcp.2008.04.001). URL <http://www.sciencedirect.com/science/article/pii/S0021999108002118>.
- [19] M Hoelzl, G T A Huijsmans, and et al. JOREK: A non-linear extended MHD code for simulating large-scale plasma instabilities and their control. *Nuclear Fusion*, XXX:in preparation, 2019.
- [20] E Franck, M Hoelzl, A Lessig, and E Sonnendrücker. Energy conservation and numerical stability for the reduced MHD models of the non-linear JOREK code. *ESAIM: M2AN*, 49(5):1331–1365, 2015. doi:[10.1051/m2an/2015014](https://doi.org/10.1051/m2an/2015014). URL <https://doi.org/10.1051/m2an/2015014>.

- [21] K. Gál, É. Belonohy, G. Kocsis, P.T. Lang, and G. Veres and. Role of shielding in modelling cryogenic deuterium pellet ablation. *Nuclear Fusion*, 48(8):085005, jul 2008. doi:[10.1088/0029-5515/48/8/085005](https://doi.org/10.1088/0029-5515/48/8/085005).
- [22] Lyman Spitzer and Richard Härm. Transport phenomena in a completely ionized gas. *Phys. Rev.*, 89:977–981, Mar 1953. doi:[10.1103/PhysRev.89.977](https://doi.org/10.1103/PhysRev.89.977). URL <https://link.aps.org/doi/10.1103/PhysRev.89.977>.
- [23] R. C. Malone, R. L. McCrory, and R. L. Morse. Indications of strongly flux-limited electron thermal conduction in laser-target experiments. *Phys. Rev. Lett.*, 34:721–724, Mar 1975. doi:[10.1103/PhysRevLett.34.721](https://doi.org/10.1103/PhysRevLett.34.721). URL <https://link.aps.org/doi/10.1103/PhysRevLett.34.721>.
- [24] P.T. Lang, A. Burckhart, M. Bernert, L. Casali, R. Fischer, O. Kardaun, G. Kocsis, M. Maraschek, A. Mlynek, B. Plöckl, M. Reich, F. Ryter, J. Schweinzer, B. Sieglin, W. Suttrop, T. Szepesi, G. Tardini, E. Wolfrum, D. Zasche, and H. Zohm and. ELM pacing and high-density operation using pellet injection in the ASDEX Upgrade all-metal-wall tokamak. *Nuclear Fusion*, 54(8):083009, jun 2014. doi:[10.1088/0029-5515/54/8/083009](https://doi.org/10.1088/0029-5515/54/8/083009).
- [25] Allen H. Boozer. Why fast magnetic reconnection is so prevalent. *Journal of Plasma Physics*, 84(1):715840102, 2018. doi:[10.1017/S0022377818000028](https://doi.org/10.1017/S0022377818000028).
- [26] F J Artola, K Lackner, G T A Huijsmans, M Hoelzl, E Nardon, and A Loarte. Understanding the reduction of the edge safety factor during hot VDEs. *Physics of Plasmas*, XXX:in preparation, 2019.
- [27] C. Sommariva, E. Nardon, P. Beyer, M. Hoelzl, and G.T.A. Huijsmans and. Electron acceleration in a JET disruption simulation. *Nuclear Fusion*, 58(10):106022, aug 2018. doi:[10.1088/1741-4326/aad47d](https://doi.org/10.1088/1741-4326/aad47d).
- [28] H. W. Müller, K. Büchl, M. Kaufmann, P. T. Lang, R. S. Lang, A. Lorenz, M. Maraschek, V. Mertens, J. Neuhauser, and ASDEX Upgrade Team. High- β plasmoid drift during pellet injection into tokamaks. *Phys. Rev. Lett.*, 83:2199–2202, Sep 1999. doi:[10.1103/PhysRevLett.83.2199](https://doi.org/10.1103/PhysRevLett.83.2199).
- [29] M Hoelzl, P Merkel, G T A Huysmans, E Nardon, E Strumberger, R McAdams, I Chapman, S Günter, and K Lackner. Coupling JOREK and STARWALL codes for non-linear resistive-wall simulations. *Journal of Physics: Conference Series*, 401:012010, dec 2012. doi:[10.1088/1742-6596/401/1/012010](https://doi.org/10.1088/1742-6596/401/1/012010).

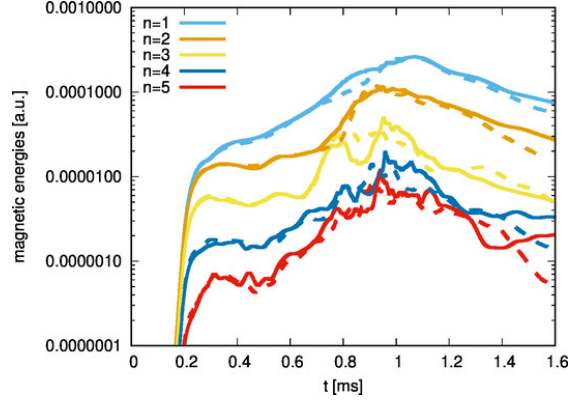


Figure 1: Comparison of the $n = 1 \dots 5$ magnetic energies between cases F and I. The color coding indicates the mode number. Solid lines correspond to case F and dashed lines to case I. Both simulations show very good agreement.

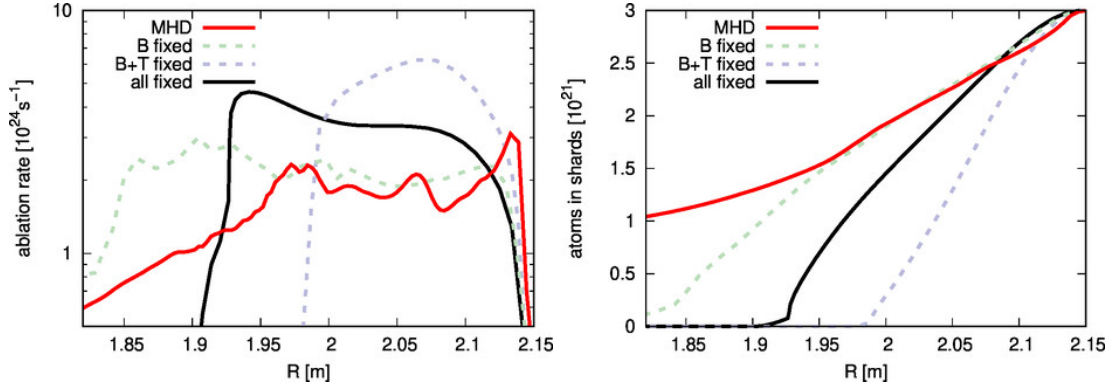


Figure 2: The ablation of several simulations is compared. Case N is shown with a red solid line, case Np with a green dashed line, case NpT with a grey dashed line, and case NpTr with a black solid line. Injection is from the right. Left: Ablation rate from the three shards injected in the cases discussed in Subsection 3.2. Right: Number of atoms left in the shards for the same simulations. Clearly, ablation is only captured correctly when the MHD activity is properly taken into account.

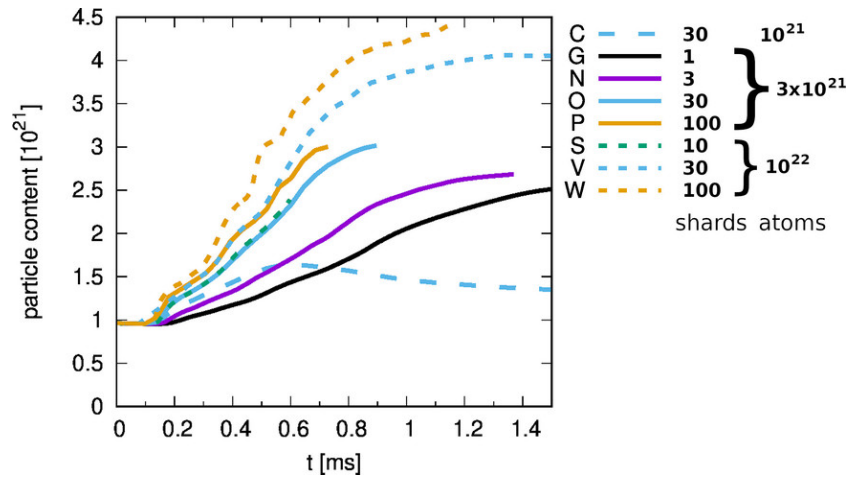


Figure 3: The plasma particle content is plotted versus the simulation time for various simulations, which differ only by the amount of injected material and the shard size (same cases as in Figure 4).

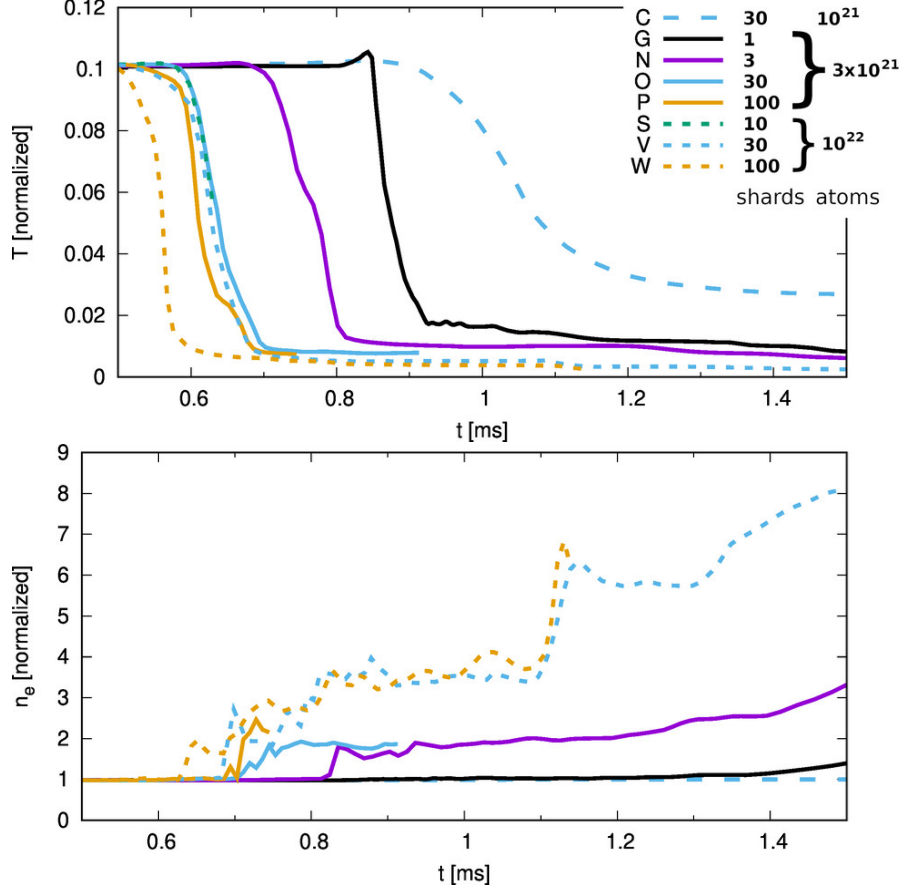


Figure 4: The core plasma temperature and density are plotted versus the simulation time for various simulations, which differ only by the amount of injected material and the shard size. Dashed lines correspond to 10^{21} injected atoms, solid lines to $3 \cdot 10^{21}$, and dotted lines to 10^{22} . The color coding is the following: single pellet in black, three shards in magenta, ten shards in green, 30 shards in blue, and 100 shards in orange. Some simulations are stopped after completion of the TQ to save computational time such that curves do not continue further.

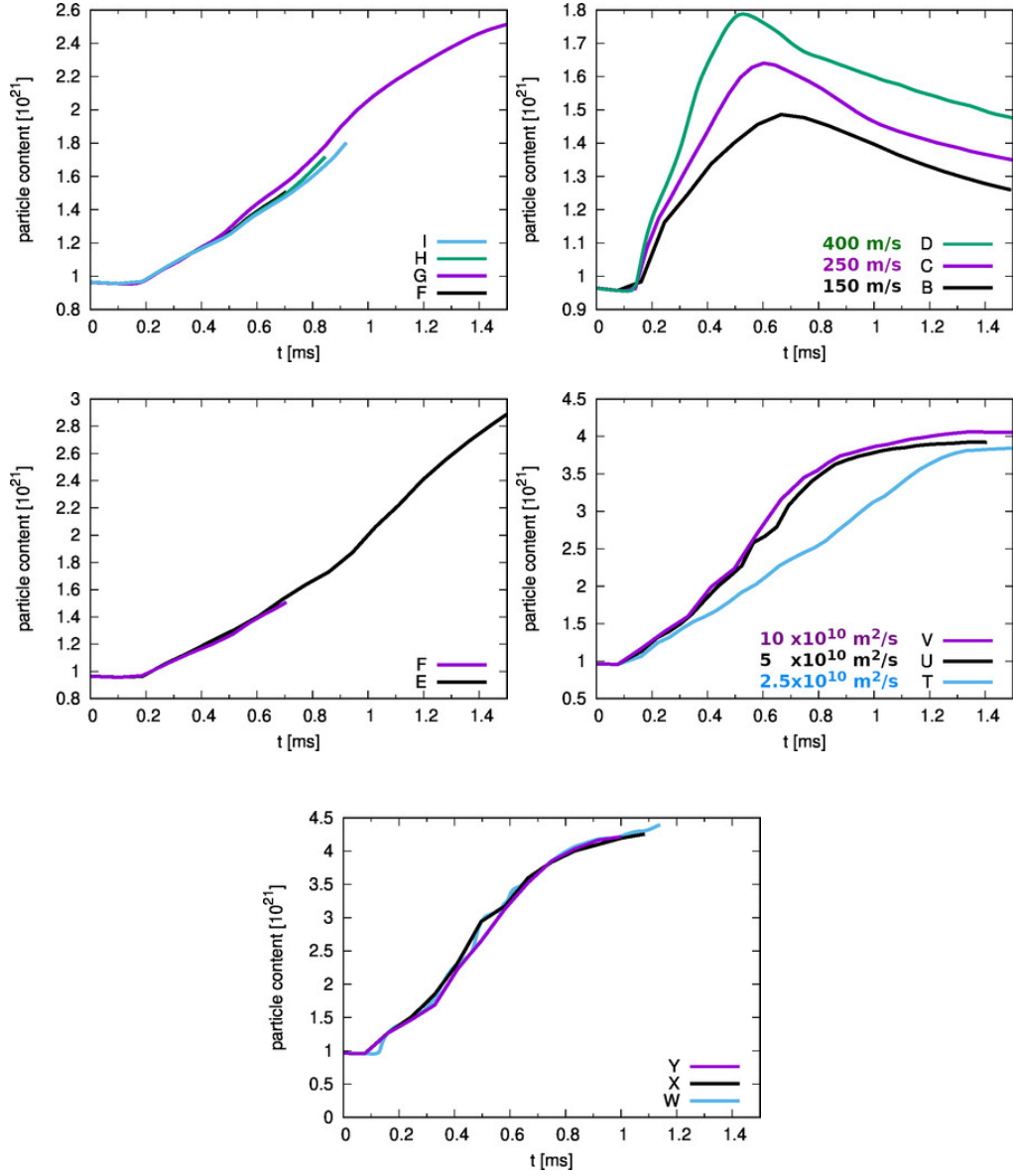


Figure 5: The plasma particle content is plotted versus the simulation time for various simulations. Top left: Simulations with different poloidal/toroidal resolutions. Top right: Different injection velocities. Mid left: Different resistivities. Mid right: Different parallel heat conductivities. Bottom: Different toroidal field amplitudes.

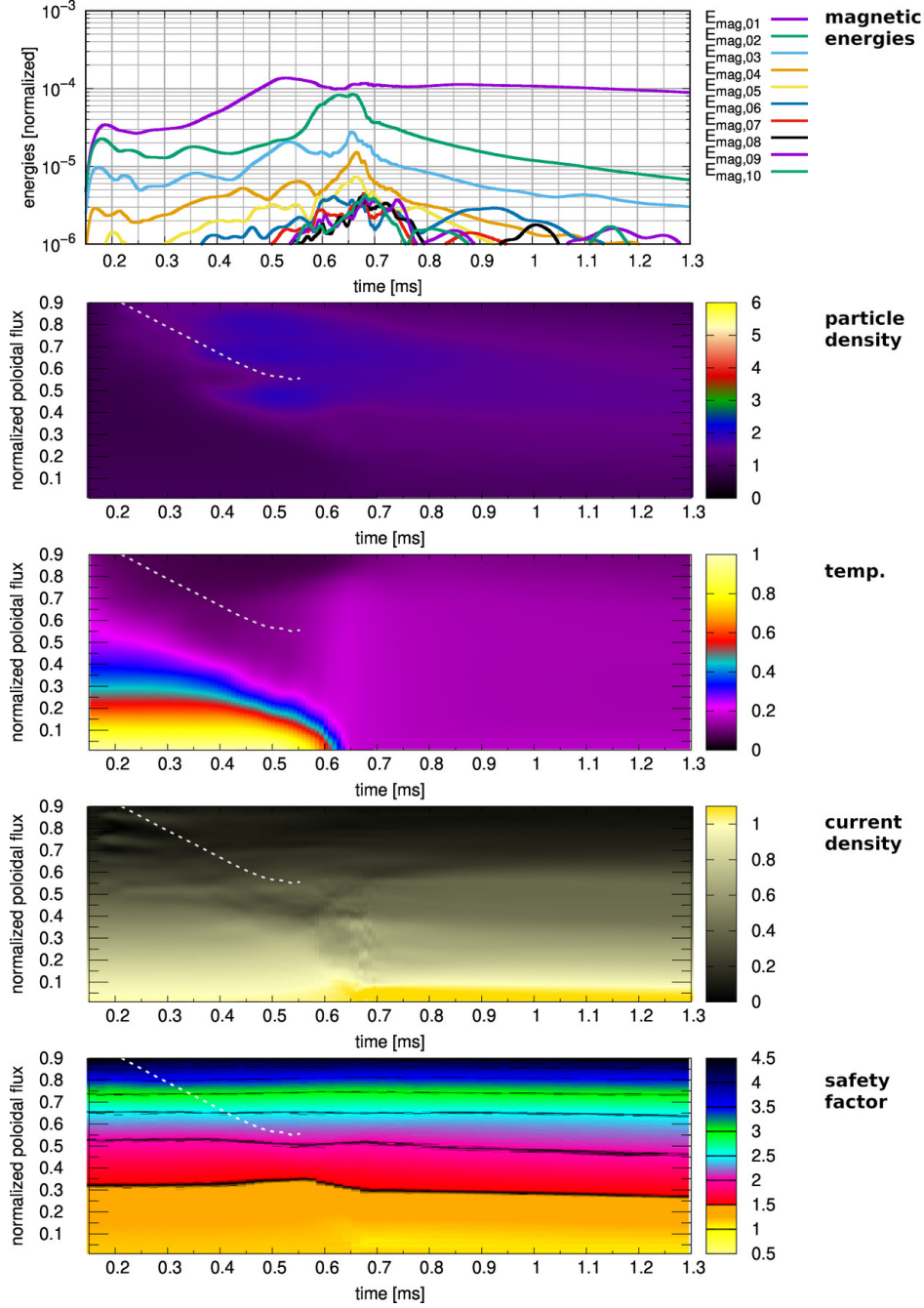


Figure 6: Overview for case D (10²¹ injected atoms, 30 shards, 400 m/s). From top to bottom, the plots show the time evolution of the magnetic energies, the density profile normalized to the initial core density, the temperature profile normalized to the initial core temperature, the current density profile normalized to the initial core current density and the profile of the safety factor q . The dashed line corresponds to the center of mass of the SPI shard cloud (until complete ablation).

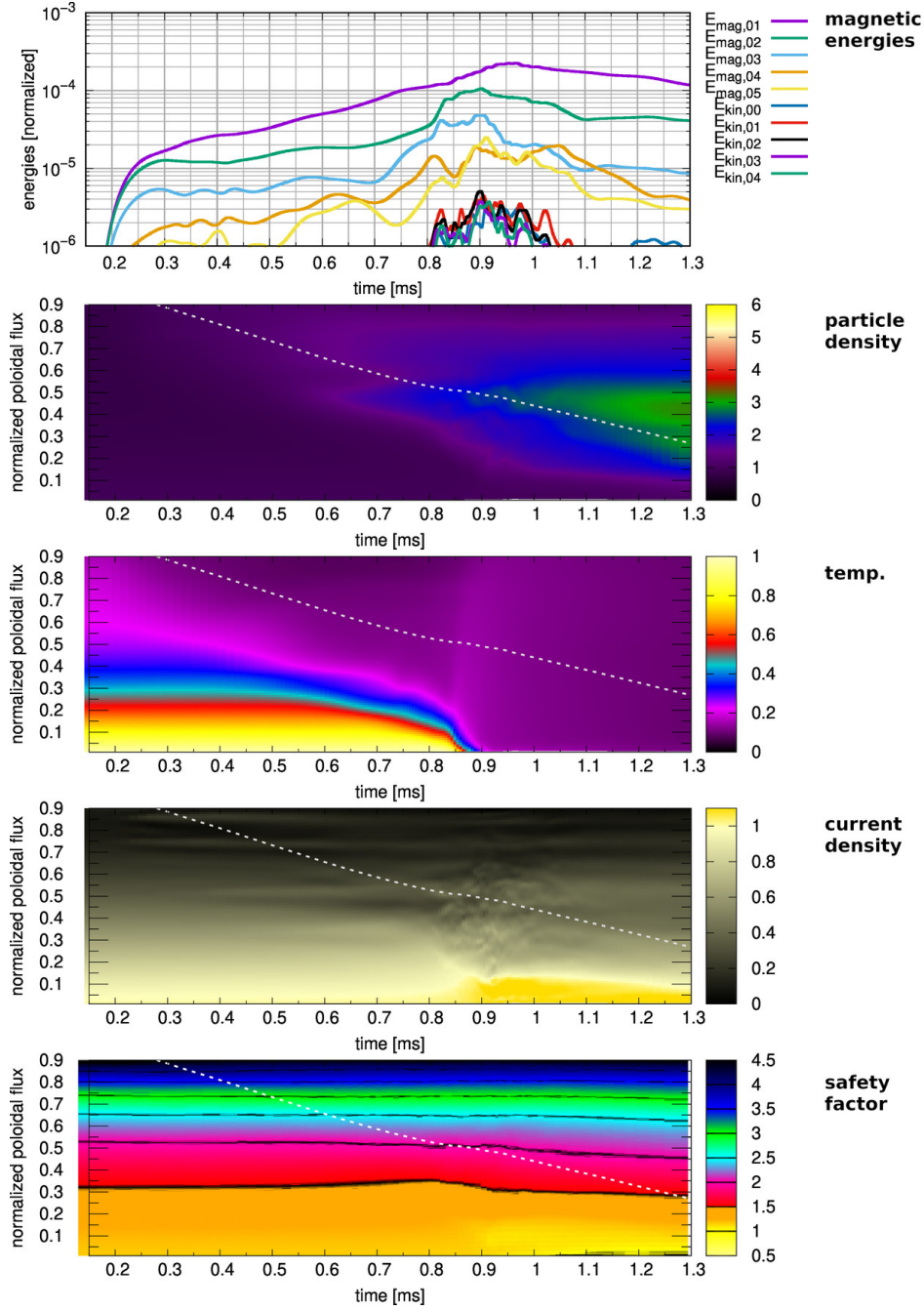


Figure 7: Overview for case G ($3 \cdot 10^{21}$ injected atoms, single shard, 250 m/s). From top to bottom, the plots show the time evolution of the magnetic energies, the density profile normalized to the initial core density, the temperature profile normalized to the initial core temperature, the current density profile normalized to the initial core current density and the profile of the safety factor q . The dashed line corresponds to the center of mass of the SPI shard cloud.

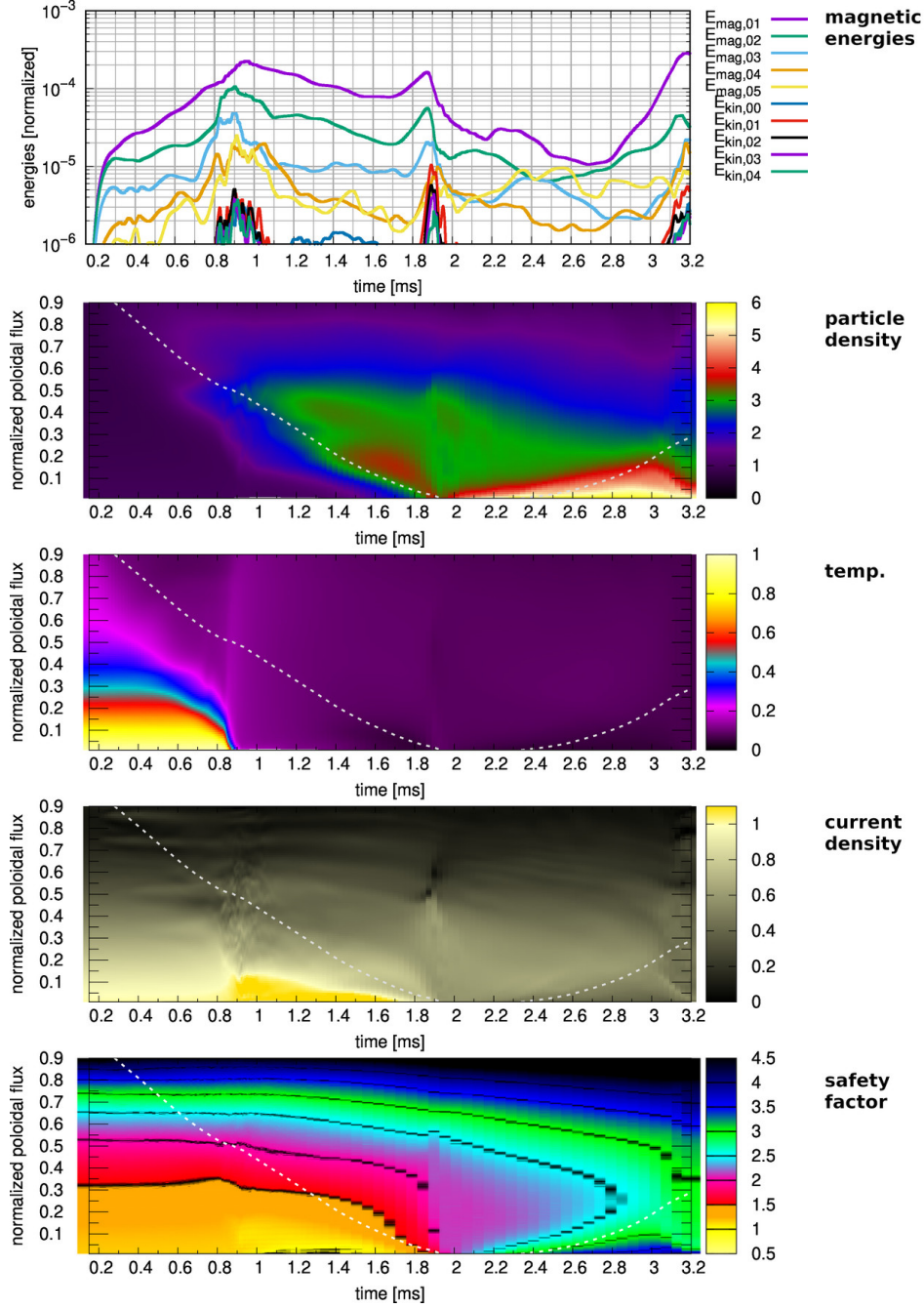


Figure 8: Overview for case G ($3 \cdot 10^{21}$ injected atoms, single shard, 250 m/s) with an extended time range. From top to bottom, the plots show the time evolution of the magnetic energies, the density profile normalized to the initial core density, the temperature profile normalized to the initial core temperature, the current density profile normalized to the initial core current density and the profile of the safety factor q . The dashed line corresponds to the center of mass of the SPI shard cloud (pellet shards cross the center).

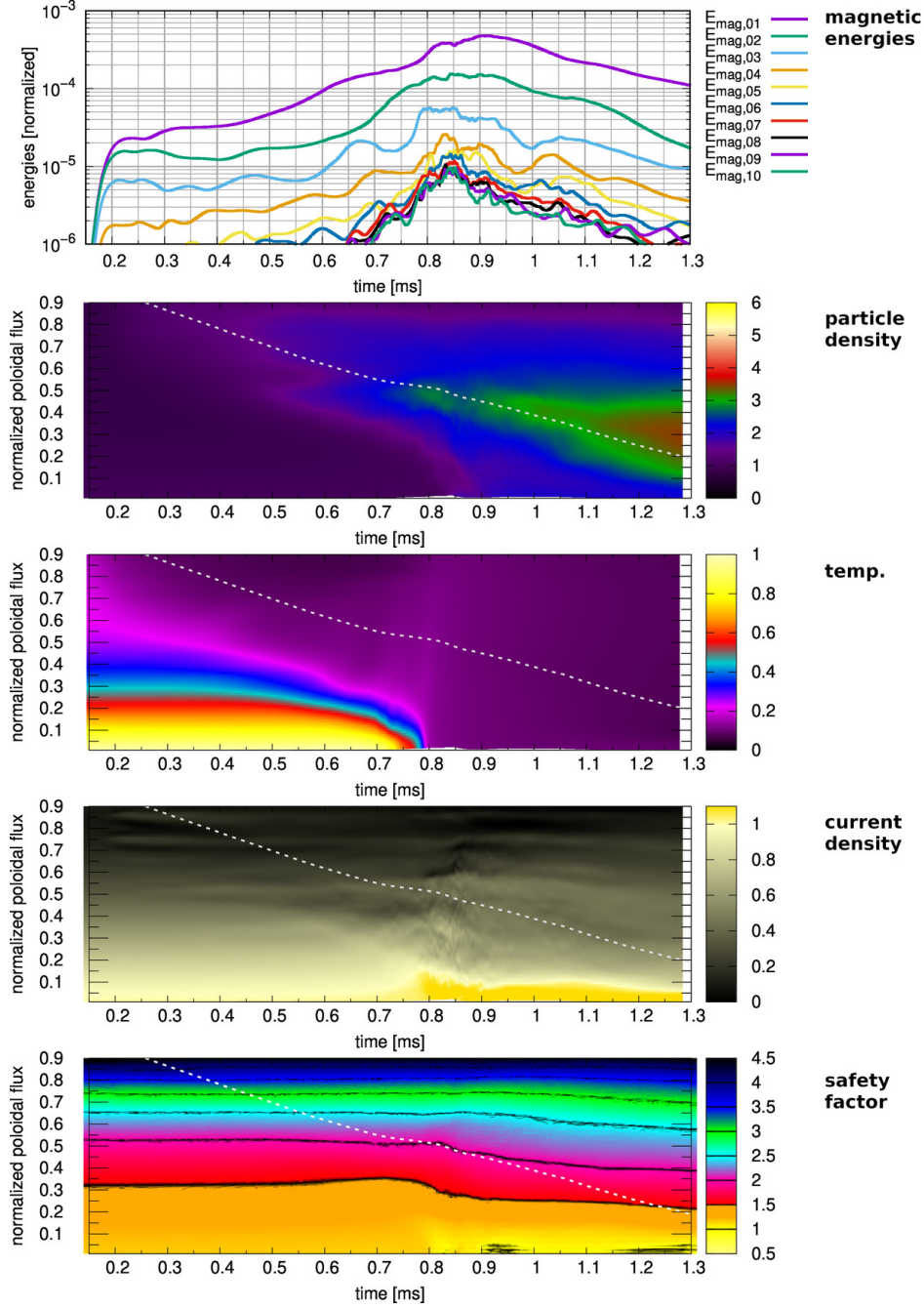


Figure 9: Overview for case N ($3 \cdot 10^{21}$ injected atoms, 3 shards, 250 m/s). From top to bottom, the plots show the time evolution of the magnetic energies, the density profile normalized to the initial core density, the temperature profile normalized to the initial core temperature, the current density profile normalized to the initial core current density and the profile of the safety factor q . The dashed line corresponds to the center of mass of the SPI shard cloud.

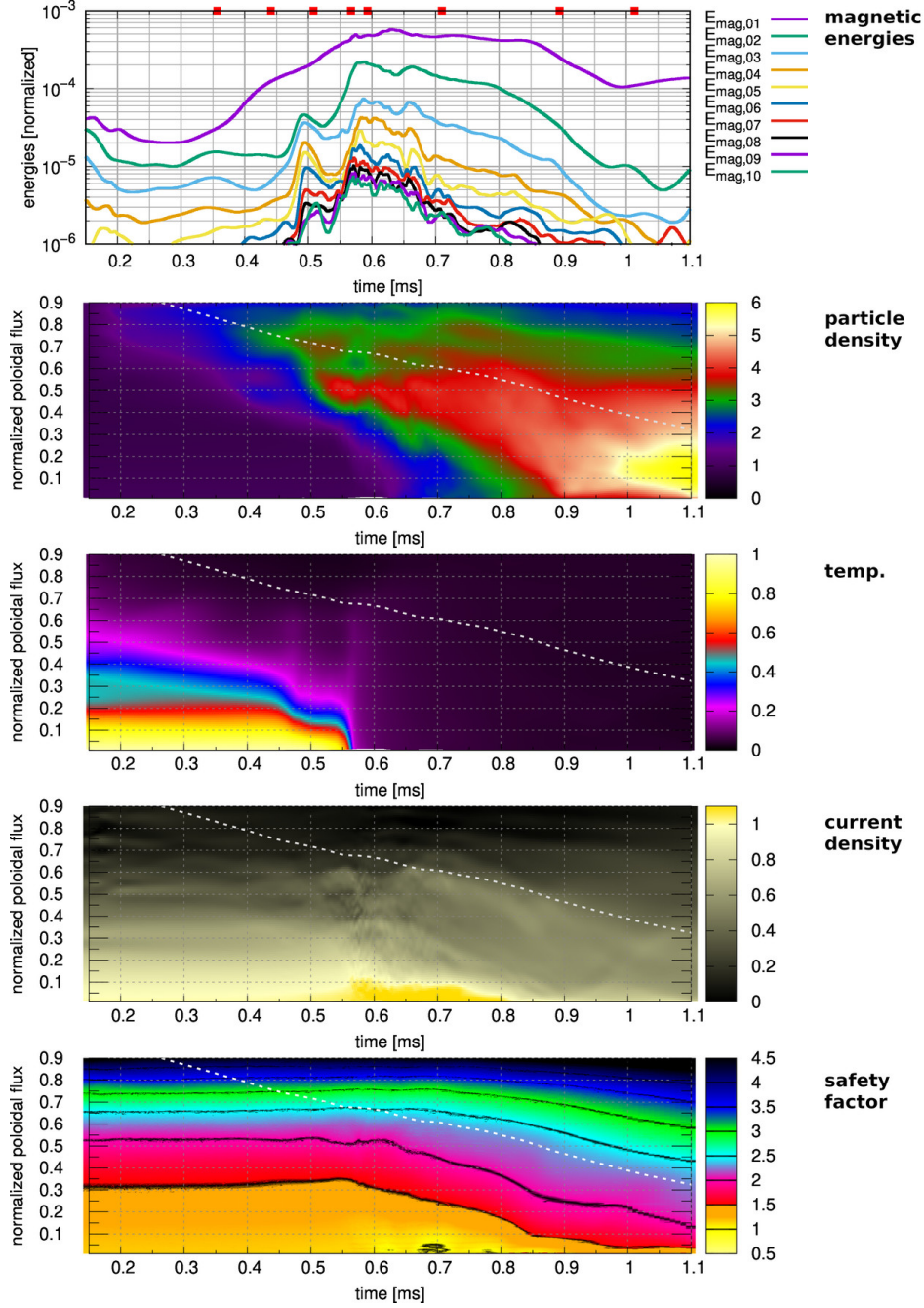


Figure 10: Overview for case W (10^{22} injected atoms, 100 shards, 250 m/s). From top to bottom, the plots show the time evolution of the magnetic energies, the density profile normalized to the initial core density, the temperature profile normalized to the initial core temperature, the current density profile normalized to the initial core current density and the profile of the safety factor q . The dashed line corresponds to the center of mass of the SPI shard cloud. The red dots indicate time points analyzed in more detail in the following Section.

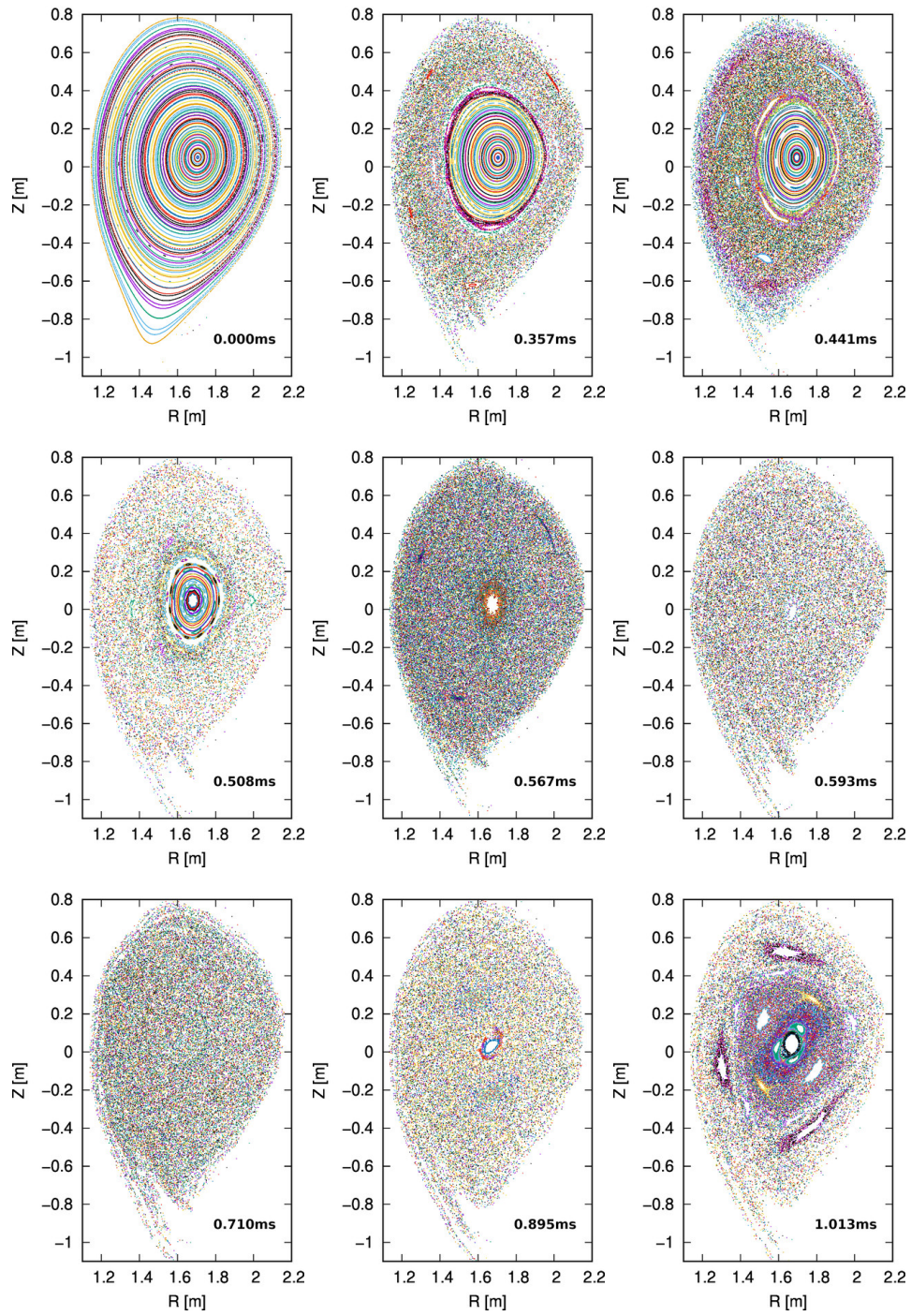


Figure 11: By Poincaré plots, the magnetic topology in case W is shown at several different points in time. These plots are created by starting 90 field lines across the whole plasma domain and tracing them for 1200 toroidal turns (or until they are lost). Time points shown are 0.000, 0.357, 0.441, 0.508, 0.567, 0.593, 0.710, 0.895, 1.013 (all times in milliseconds).

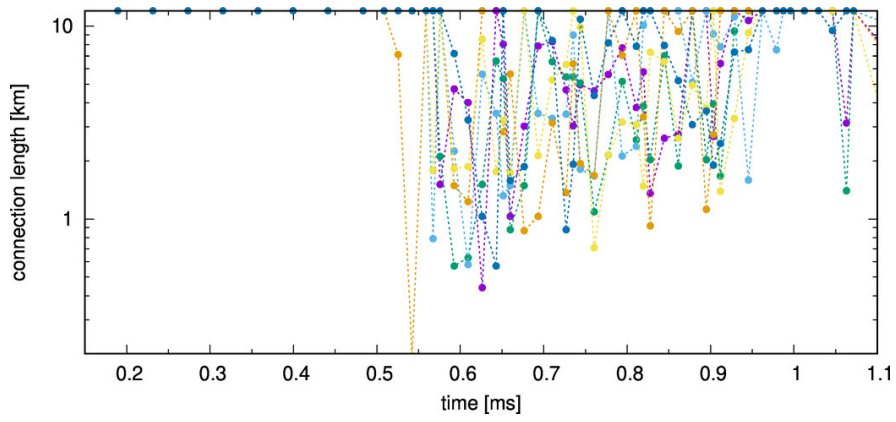


Figure 12: Case W. For six field lines started very close to the magnetic axis, the connection length to the divertor target is plotted versus time (maximum value of 12 km since the field line tracing is stopped then).

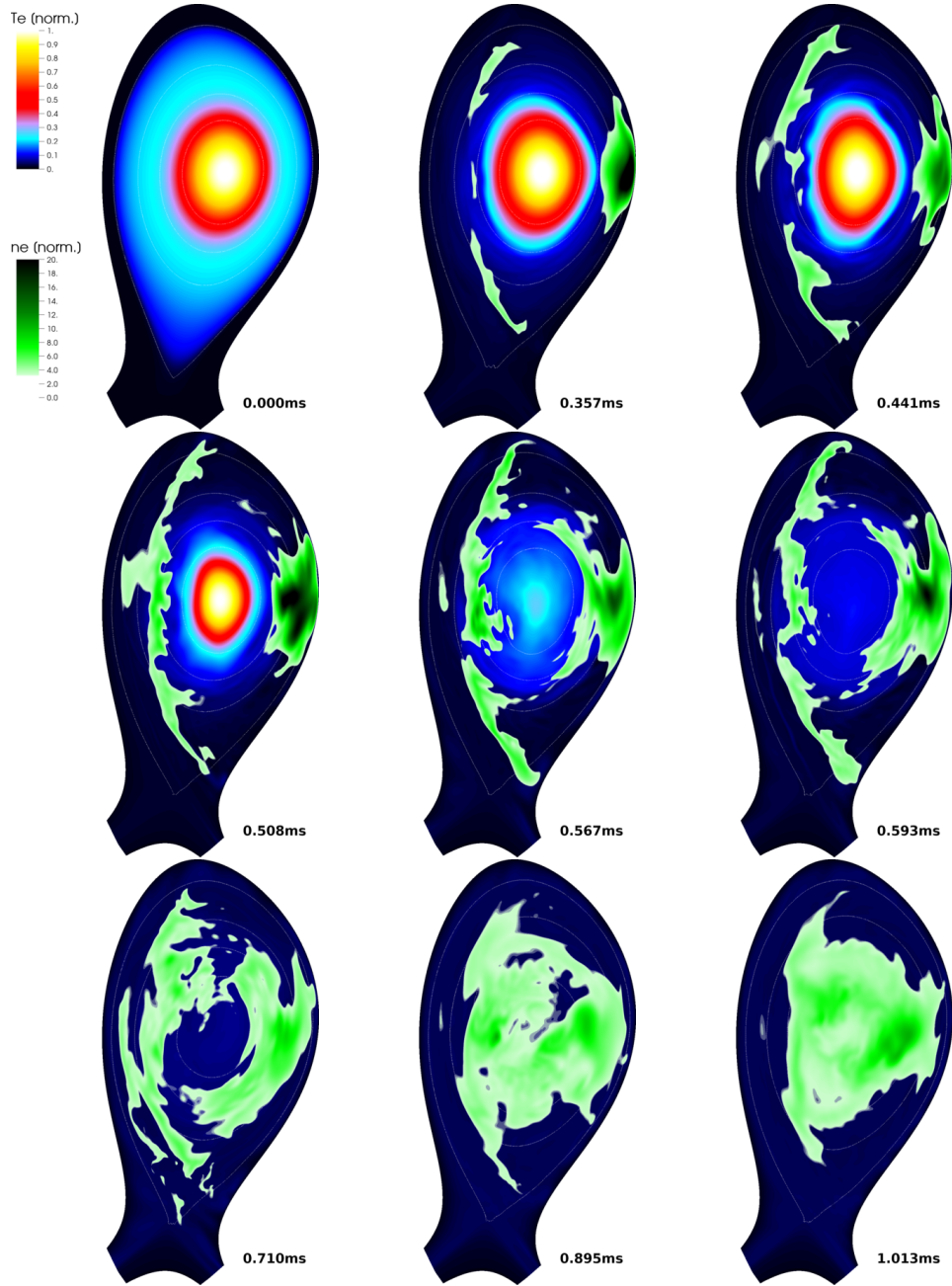


Figure 13: Density and temperature distributions are plotted for case W at the toroidal location $\phi = 0$. Time points shown are the same as in Figure 11: 0.000, 0.357, 0.441, 0.508, 0.567, 0.593, 0.710, 0.895, 1.013 (all in milliseconds).

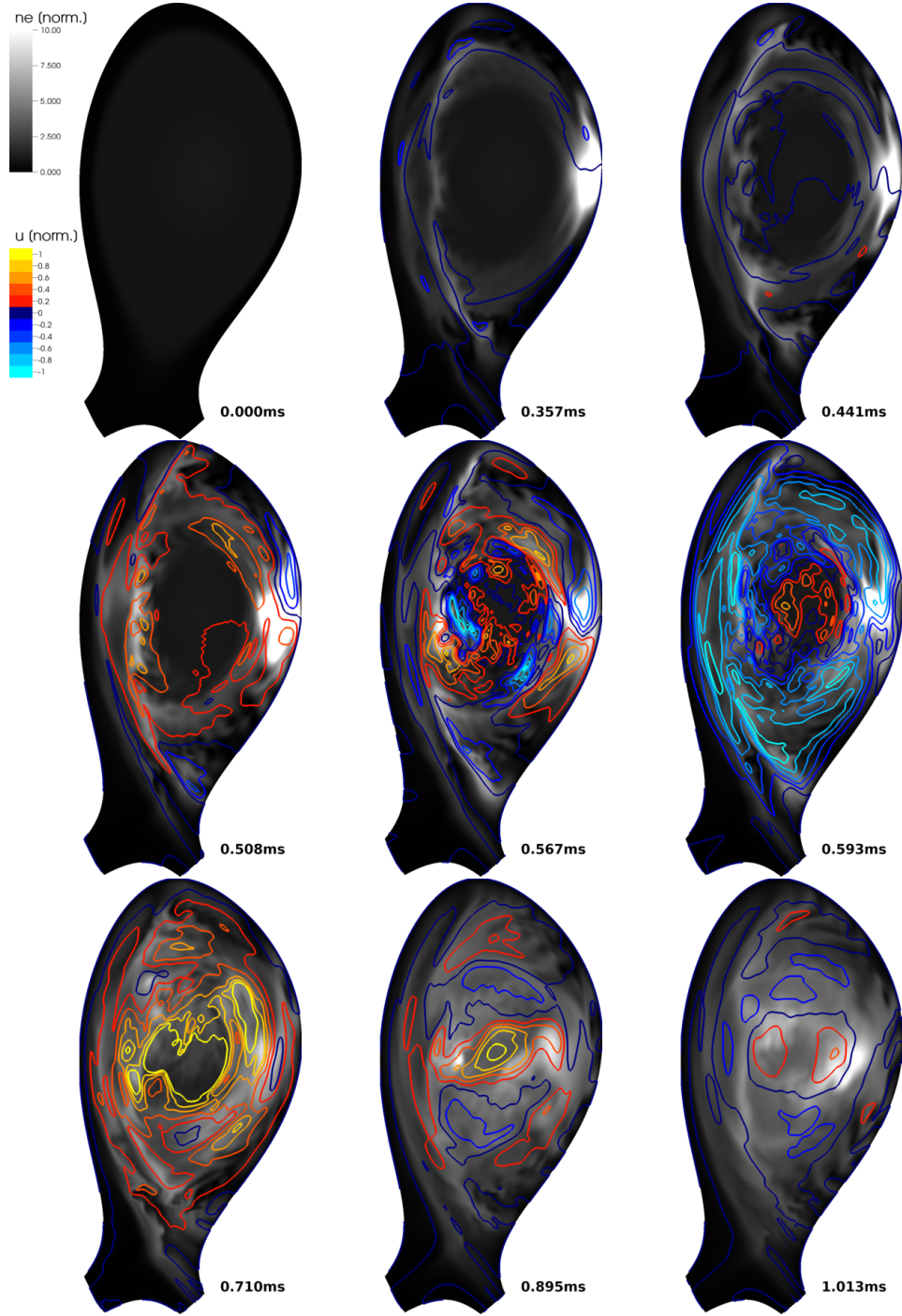


Figure 14: For case W, the density distribution is shown in black and white. Contours of u , the stream function of the perpendicular plasma velocity, are plotted in color. Time points shown are the same as in Figure 11 and 13: 0.000, 0.357, 0.441, 0.508, 0.567, 0.593, 0.710, 0.895, 1.013 (all in milliseconds). An outwards oriented convection cell is observed in the high density region whenever heat is released from the plasma core such that the pressure of the ablation cloud is suddenly increased. This is particularly visible at 0.567ms, which corresponds to the core 34Q time. After the TQ, a strong poloidal rotation induced by Maxwell stress is visible ($t=0.710$ ms), which supports the re-healing of flux surfaces by decoupling MHD modes at different radial locations.